

Molecular Dynamics Study of Carbon Nanotubes/Polyamide Reverse Osmosis Membranes: Polymerization, Structure, and Hydration

Takumi Araki,^{†,§} Rodolfo Cruz-Silva,[†] Syogo Tejima,^{†,§} Kenji Takeuchi,^{†,‡} Takuya Hayashi,^{†,‡} Shigeki Inukai,[†] Toru Noguchi,^{†,‡} Akihiko Tanioka,[†] Takeyuki Kawaguchi,[†] Mauricio Terrones,^{‡,||} and Morinobu Endo^{*,†,‡}

[†]Global Aqua Innovation Center, Shinshu University; 4-17-1 Wakasato, Nagano 380-8553, Japan

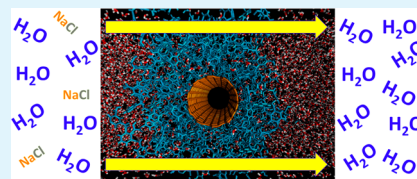
[‡]Institute of Carbon Science and Technology, Shinshu University; 4-17-1 Wakasato, Nagano 380-8553, Japan

[§]Research Organization for Information Science & Technology, 2-32-3, Kitashinagawa, Shinagawa-ku, Tokyo, 140-0001, Japan

^{||}Department of Physics, Chemistry and Materials Science and Engineering, and Center for 2-Dimensional and Layered Materials, The Pennsylvania State University; University Park, Pennsylvania 16802, United States

Supporting Information

ABSTRACT: Carbon nanotubes/polyamide (PA) nanocomposite thin films have become very attractive as reverse osmosis (RO) membranes. In this work, we used molecular dynamics to simulate the influence of single walled carbon nanotubes (SWCNTs) in the polyamide molecular structure as a model case of a carbon nanotubes/polyamide nanocomposite RO membrane. It was found that the addition of SWCNTs decreases the pore size of the composite membrane and increases the Na and Cl ion rejection. Analysis of the radial distribution function of water confined in the pores of the membranes shows that SWCNT+PA nanocomposite membranes also exhibit smaller clusters of water molecules within the membrane, thus suggesting a dense membrane structure (SWCNT+PA composite membranes were 3.9% denser than bare PA). The results provide new insights into the fabrication of novel membranes reinforced with tubular structures for enhanced desalination performance.



KEYWORDS: nanocomposite membrane, desalination, diffusion, polymer network, molecular dynamics, radial distribution

1. INTRODUCTION

Water desalination has become one of the most important challenges in the 21st century.^{1,2} Climate change, water pollution, and urban development in arid areas are some of the main reasons that have fueled the development of new desalination technologies, such as reverse osmosis (RO) membranes,³ membrane distillation,⁴ evaporation distillation,⁵ geothermal desalination,⁶ and solar desalination.⁷ Among these proven technologies and several others under development, RO desalination has become the most reliable method currently in use and is the subject of intense research. Since Loeb and Srinivasan developed the first cellulose acetate membranes with high water flux and operation pressure sufficiently low to become commercially feasible, many other polymers have been studied. In the late 70s, a breakthrough in RO technology was achieved when John Cadotte developed the interfacial synthesis of polyamide (PA) membranes,⁸ resulting in a large family of membranes whose separation properties range from high flow nanofiltration to high desalination performance. PA membranes are usually prepared by reacting a polyfunctional amine compound dissolved in an aqueous phase with a diacyl or triacyl chloride monomer dissolved in the organic phase. Thus, by changing the type of monomers or the mixture of monomers on each phase, an infinite number of structures are potentially available. However, regardless of the structure, most PA membrane performance falls within a well-known trade-off

between flow and salt rejection, i.e., high-flow membranes show lower desalination performance whereas membranes with high salt rejection usually have lower flow.^{9–11} Several studies have reported the effect of network topology on the flux and desalination performance.^{10,11} The effect of cross-linking or ordered network is not the same for all materials. For example, it has been found that a small amount of cross-linking introduces porosity to linear PA and consequently increases the permeation, but excessive cross-linking can sometimes decrease the water flux due to the difficulty of the membrane to swell.^{9,12} In this context, the introduction of disordered nodes using polyamine polymers has been shown to positively influence both the desalination and flux performance in fully aromatic PA membranes.¹¹

Nowadays, computer simulations are becoming an effective tool to screen all these possibilities to guide the preparation of membranes and study their performance at the nanoscale. This rational approach started in the mid-1990s with the pioneering work of Murad, who used a computational approach to calculate diffusion coefficients and osmotic pressures as well as the density profiles of both the solute and solvent molecules in different materials used for RO membranes.^{13,14} These studies

Received: July 11, 2015

Accepted: October 20, 2015

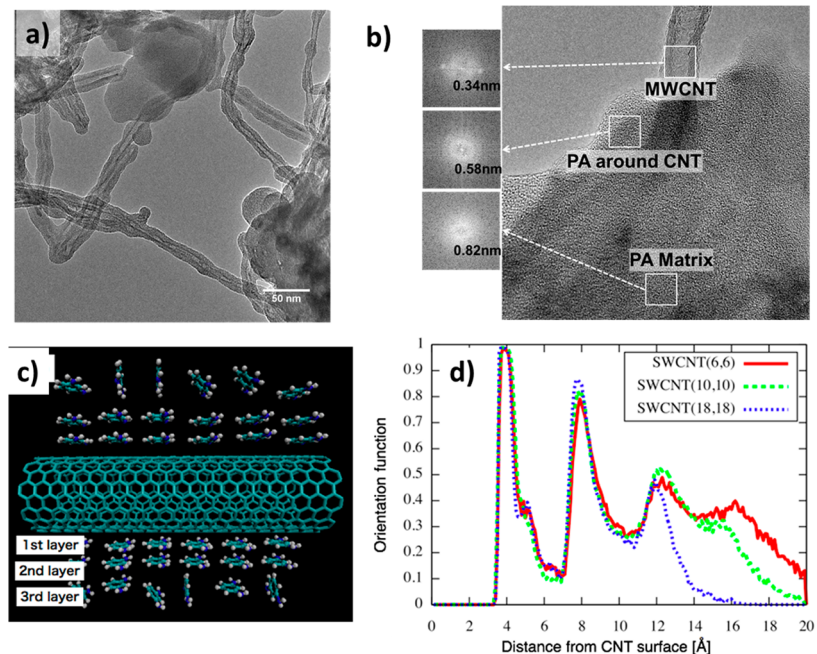


Figure 1. (a) Transmission electron microscope (TEM) image of MWCNT+PA carried out in a low monomer concentration. MWCNTs are coated with a thick layer of PA. (b) TEM image showing the MWCNT+PA reverse osmosis membrane. The insets correspond to the fast Fourier transform (FFT) of several areas, suggesting different structures of the PA in different areas of the image. (c) Scheme illustrating the orientation of the first three layers of MPD molecules on the surface of the SWCNT, and d) plot of the orientation function of MPD molecules adsorbed on SWCNT of different diameters as a function of their distance to the SWCNT surface.

were followed shortly by the simulation of the most successful desalination membrane to date, FT-30, derived from the cross-linking reaction of 1,3-diaminobenzene (MPD) and 1,3,5-benzenetricarbonyl trichloride (TMC).^{15,16} In these works, the simulation was used to understand the diffusion process and the effect of cross-linking density. Ding et al.¹⁷ correlated the effect of free-volume with the heterogeneous distribution of water through molecular dynamics (MD). The hydration of the PA membrane by MD calculations has been studied over the last few years. First, a simple model was used,¹⁶ and more recently, a more accurate model that includes residual carboxylic groups has been developed.¹² It is clear that MD has become a useful tool to understand the performance not only of plain polymer membranes but also nanocomposite RO membranes, such as those containing silica nanoparticles¹⁸ or carbon nanotubes.¹⁹ Indeed, MD have also been used to simulate the water transport on different nanomaterials with nanochannels, such as zeolites,²⁰ boron nitride layers,²¹ and carbon nanotubes^{22,23} as well as graphene oxide²⁴ and graphene membranes.^{25,26}

To date, several groups have studied the performance of RO nanocomposite membranes made of polyamide/carbon nanotubes.^{19,27–33} However, the reported approaches have been mainly empirical in nature, and there is still no clear understanding of the behavior of such nanocomposite films. Most of the studies dealing with membrane molecular dynamics have focused on the transport of water within the carbon nanotubes while disregarding the changes in the polymer matrix due to the presence of carbon nanotubes. However, it is well-known that nanofillers strongly modify polymer matrix properties, such as chain mobility, hardness, molecular transitions, diffusion, and consequently the water transport. This theoretical work provides new insights on single walled carbon nanotubes (SWCNT)+PA membranes, as a model case of a CNT nanocomposite RO membrane, for desalination

applications. In particular, we focused on the effect of carbon nanotubes, particularly SWCNTs, on the membrane structure and its hydration behavior.

2. RESULTS AND DISCUSSION

2.1. MPD Adsorption on the Multiwalled Carbon Nanotube (MWCNT) Walls. Under our experimental conditions used to prepare MWCNT+PA nanocomposite membranes,³³ typically, carbon nanotubes are dispersed in water-based MPD solutions. The carbon nanotubes interact with the MPD molecules because of the strong π - π interactions and van der Waals forces. We experimentally found that when mixing an aqueous solution containing 2 wt % of MPD and 0.4 wt % of MWCNT, approximately 16.3% of the monomer adsorbed on the surface of the nanotubes (Figure S1a). Indeed, we found a strong affinity between the PA and the MWCNT, and when the polymerization reaction was carried out under low MPD monomer concentration, most of the resulting PA was strongly attached to the walls of the MWCNT, as shown on Figure 1a. When the transmission electron microscope (TEM) images of these PA-coated MWCNTs were examined in detail, we found a different order on the vicinity of the nanotubes (Figure S2) of a PA layer surrounding the carbon nanotube. Apparently, larger-ordered structures characterized by banded contrast areas can be observed in these samples (Figure S2a–c) that are different from the less-ordered structure shown by the polymer in the bulk (Figure S2d). Figure 1b shows a typical TEM image of MWCNT+PA nanocomposite membranes prepared by interfacial polymerization.

PA network derived from the reaction of MPD and TMC in the absence of carbon nanotubes can be described as a highly cross-linked network in which each MPD molecule binds two TMC moieties, and each TMC moiety is bonded to three MPD

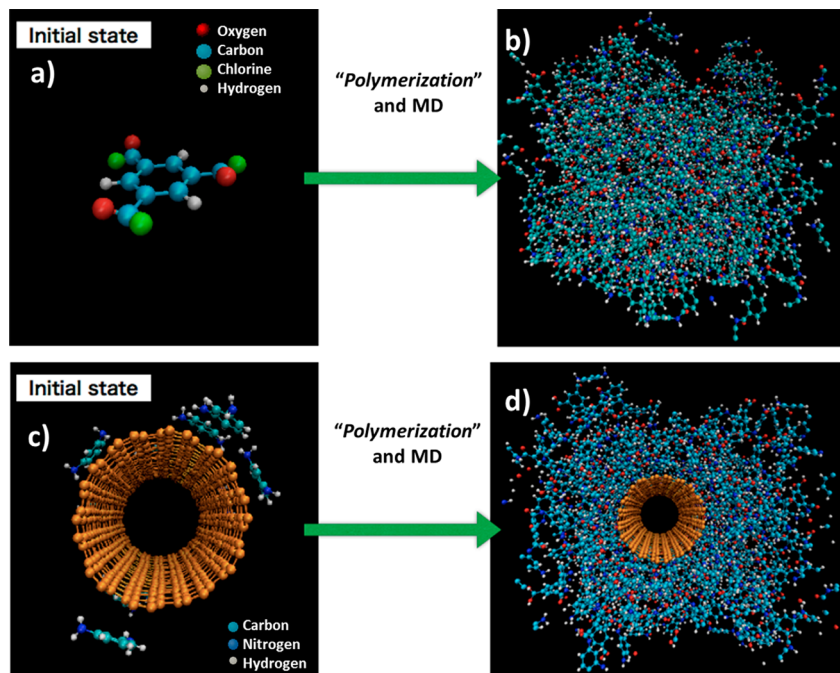


Figure 2. Two different methods were used to build the PA structure. In brief, the plain PA membrane model was derived starting with a single TMC molecule, shown in (a) and adding MPD and TMC molecules without major constraints; (b) shows the resulting PA molecule after MD relaxation. Conversely, the initial state of the SWCNT+PA nanocomposite membrane is shown in (c) and consists of 10 MPD molecules absorbed and oriented on the surface of the SWCNT; (d) shows the resulting SWCNT+PA membrane after polymerization and MD relaxation.

moieties as shown in Figure S1b. However, when the PA network is examined on a larger scale, it is clear that the structure of this network can be very complex, ranging from a highly branched network with low cross-linking degree (Figure S3a) to a highly cross-linked and regular network (Figure S3b). In addition, the presence of rings with strained bonds can also be expected (Figure S3c). These rings can even be part of an ordered network as shown in Figure S3d. It is noteworthy that network structure (or topology) strongly influences the bond geometry and, consequently, some properties such as the porosity, density, and swelling capability. These parameters result in significant effects on water desalination and permeation properties.¹⁰

Although the difference in the polymer microstructure around the MWCNTs seen by TEM in Figure 1b is less evident than in Figure 1a and Figure S2a–c, mainly due to the interference of the bulk polymer during the observation, the FFT analysis of the PA network in the surrounding areas of the MWCNT compared to that of the PA matrix still show clear differences. Such a change in the structure presumably arises from the influence of the MWCNT during PA synthesis, and for this reason, we studied the influence of a SWCNT as a model of a carbon nanotube on the adsorption and subsequent cross-linking reaction. We choose this type of carbon nanotube because the molecular dynamics of very large structures, such as a MWCNT, is restricted due to their large number of atoms. In our case, there is no covalent bonding between the polymer and the nanotube; thus, the interactions and dynamics between the monomers and the polymer with the SWCNT walls can be compared to those obtained with MWCNTs because these interactions correspond mainly to strong van der Waals forces with the outer wall.

In particular, we carried out theoretical simulations using armchair SWCNTs with different diameters and found that the monomers self-organize in a preferred orientation as a function

of their distance to the nanotube wall. Figure 1c shows such orientation schematically, which is analytically plotted in Figure 1d. It was found that the first and second layer of MPD monomers are preferentially arranged in a parallel way to the surface; however, the third layer exhibited a random orientation. Regardless of the nanotube diameter, the first orientation layer peak was located at 3.9 Å and exhibited a high orientation degree. A second layer of monomers at 8.0 Å was found, though its orientation decreased slightly as compared to the first layer. Interestingly, the orientation of this second monomer layer was sensitive to the nanotubes diameter and increased as the diameter of the simulated nanotube became larger. Conversely, a third layer of disordered MPD molecules was found at approximately 12.3 Å. The lack of orientation of this layer is explained because the SWCNT-MPD interactions are mainly due to van der Waals forces, which decrease considerably as the distance increases but are very strong within a short distance range.³⁴ We must point out that these calculations were carried out considering only the MPD-SWCNT interactions, but we also compared simulations with and without water (Figure S4b and Figure 4a, respectively), and we found that there was no significant change in the orientation (Figure S4c) of MPD molecules. No other differences were found in the MPD adsorption behavior for different nanotube diameters; therefore, we will consider only the SWCNT(10,10) as a model for constructing the SWCNT+PA nanocomposite RO membrane.

2.2. Influence of the SWCNT on the Cross-Linking Reaction. Next, we studied through molecular mechanics the influence of a SWCNT during the polymerization of the MPD and TMC monomers and the resulting PA networks. The restrictions during the "polymerization" algorithm are detailed in the Experimental Section and schematized in Figure S5. The same method was applied for building both the plain PA and SWCNT+PA membranes; however, the initial conditions were

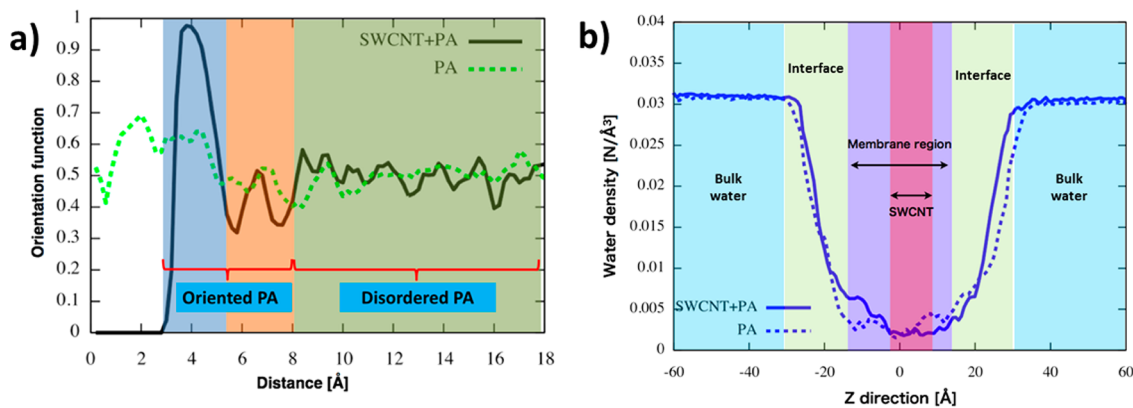


Figure 3. (a) Orientation functions for the SWCNT+PA nanocomposite membrane model and the plain PA membrane. (b) Water density for z direction in both membranes after hydration. The purple region is defined as the membrane region for both types of membranes, whereas the wine-colored area indicates the vertical position of the SWCNT in the nanocomposite membrane.

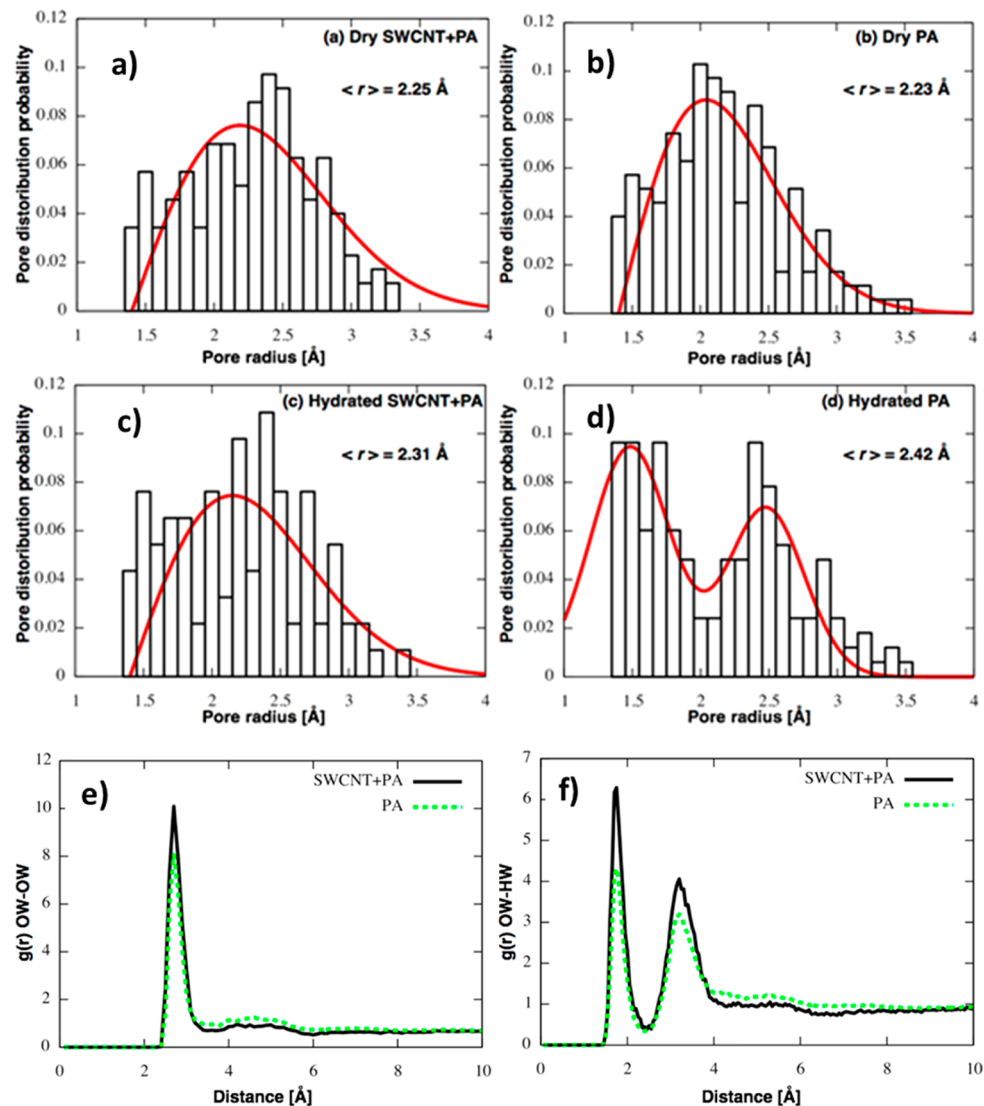


Figure 4. Pore-size distributions of the dry and hydrated membranes. (a) Dry SWCNT+PA membrane, (b) dry plain PA membrane, (c) hydrated SWCNT+PA membrane, and (d) hydrated plain PA membrane. From the hydrated SWCNT+PA and plain PA membranes, the radial distribution functions of (e) oxygen–oxygen (OW–OW) and f) oxygen–hydrogen (OW–HW) were calculated.

different. We started the polymerization of the plain PA membrane with a single TMC molecule as a seed (Figure 2a) and added 265 MPD and 212 TMC molecules by using the

steps indicated in Figure S5a–d. The polymerization mechanism corrects any overlapping molecule (Figure S5b and c) and allows self-cross-linking of the neighboring TMC

and MPD reactive groups (Figure S5e), resulting in ring formations, mainly with 4 or 6 units (Figure S6a and b, respectively). These rings represent real features of the PA polymer. The polymerization method also restricts the polymerization to the simulation box limits (Figure S5f) by controlling the reactivity outside the simulation box. In both cases after the “polymerization” stage, we “hydrolyzed” the residual acyl chloride functionalities by substituting them with a hydroxyl group, as shown in Figure S5g, and performed 10000 MD steps with a time step of 0.1 fs to reach the minimum energy configuration and reduce the unit cell length by 0.1 Å increments for atomic mass density control.³⁶ The resulting PA has a cross-linked structure, and Figure 2b shows a snapshot of the membrane after MD. Conversely, for the polymerization in the presence of the SWCNT, the initial state (Figure 2c) consisted of a SWCNT(10,10), 5 nm in length and 840 carbon atoms where 10 MPD molecules were adsorbed on its surface. Then, we added 226 MPD and 183 TMC to reach the final state shown in Figure 2d. The mass ratio of SWCNT to PA is ~14.98%, which was targeted based on our experimental results.

To study the influence of the SWCNT in the network geometry, we calculated the orientation of the aromatic moieties as a function of the distance to the nanotube and compared these values to those from the plain PA membrane (Figure 3a). The latter showed values fluctuating around 0.5, suggesting a random orientation of the network, as expected. Conversely, the SWCNT+PA exhibited a highly oriented layer, highlighted in blue in Figure 3a, with a peak at 3.8 Å. This peak is similar to that found by absorption and shown in Figure 1d and indicates that during polymerization the strongly attached first layer kept the same orientation. However, a second layer with a preferred perpendicular orientation is shown. The orientation of this layer contrasts to the parallel orientation in the adsorbed monomer case (see Figure 1d) and most likely was induced by the bond geometry after cross-linking with the first layer that is strongly attached to the SWCNT. This layer is extending from approximately 5 to 8 Å, shows orientation function values between 0.25 and 0.45, and is shown in orange in Figure 3a. Farther areas of the nanocomposite membrane (indicated in green) had a disordered structure topologically similar to the plain PA. However, it is clear that the SWCNT constraint might be acting as a seed that developed a specially oriented network in its vicinity. This orientation could well be induced by the strong van der Waals forces between the SWCNT and the aromatic monomers on its surface.

2.3. Membrane Hydration. We investigated the hydration behavior and water diffusion on the SWCNT+PA and plain PA membrane models. For the SWCNT+PA membrane, we used a periodic cell that results in a SWCNT of infinite length and, therefore, there is no water permeation into the nanotube. Several groups have discussed the possibility of water flow inside the nanotubes;^{19,22,23} however, as-synthesized SWCNTs have caps that prevent the water flow along the hollow core of the nanotube, and MWCNT usually have bridges that also block the flow of water within the nanotube. For simulating water contact, 4000 water molecules were set on top and bottom of the membrane along the z axis and left to equilibrate with the membrane for 4 ns. Figure 3b shows the resulting water density along the z axis (perpendicular to the membrane) for the SWCNT+PA and plain PA cases. The bulk water region is colored in cyan, and the interface between the membrane and bulk water is indicated in light green. The interface has a linear

gradient water density from the bulk values ($0.03 \text{ N}/\text{\AA}^3$) to those typical of the PA membrane ($\sim 0.003 \text{ N}/\text{\AA}^3$). The area closer to the SWCNT displayed similar water densities to that of the plain PA; thus, the SWCNT did not restrict the water density on its vicinities.

Figure 4 shows the pore-size distributions in the dry and hydrated membranes were estimated by locally probing the free-space using a particle size with a specific radius.³⁵ We estimated the volume occupied per atom as a sphere with a van der Waals radius and excluded this atomic volume. For the SWCNT+PA membrane, the analysis excluded the cylindrical space corresponding to the nanotube. In the dry conditions, both the SWCNT+PA (Figure 4a) and PA (Figure 4b) membranes showed similar average pore-sizes of 2.25 and 2.23 Å radius, respectively. Even though the pore radii of SWCNT+PA and PA membrane were similar, the total pore number is smaller in the SWCNT+PA case, thus suggesting a dense and more homogeneous membrane. This result shows that the total free-volume decreased by the van der Waals interaction with the SWCNT. Panels c and d in Figure 4 show the pore-size distributions of both membranes after hydration. Here, notably, differences arose; although the plain PA membrane developed a bimodal pore-size distribution with peaks at 1.5 and 2.5 Å, the SWCNT+PA kept its monomodal pore-size distribution. The hydration behavior of the plain PA membrane agrees with the bimodal pore distribution found by Harder³⁶ and supports the accuracy of our membrane-building algorithm. Free spaces within the plain PA membrane are changed easily by hydration, which are responsible for generating water clusters and zones with lower density.³⁷ Average pore diameter of the plain PA case is 4.84 Å, and these values are near the experimental value of 5.1 Å, as reported.³⁸

Table 1 shows the density of PA in dry and hydrated states. For SWCNT+PA, we estimated the density by excluding the

Table 1. Mass Density of Dry and Hydrated PA Membrane and the SWCNT+PA Nanocomposite Membrane with the Calculation Excluding the Large Pore and SWCNT Region

membrane type	PA atomic density, g/cm ³
SWCNT+PA (dry)	1.35
PA (dry)	1.33
SWCNT+PA (hydrated)	1.32
PA (hydrated)	1.27

SWCNT region. The hydrated PA membrane value is near the FT-30 membrane density experimentally reported,³⁹ whereas the density of the SWCNT+PA membrane is slightly higher. For both membranes, density decreased after hydration, as expected; however, the density reduction for the SWCNT+PA membrane was ~5% smaller than that of the plain PA membrane. The reduction in hydration capability most likely originated by the smaller free-volume available, which originated because of better molecular packing.

In Figure 4e and f is shown the radial distribution functions of water within the hydrated membranes. Figure 4e describes the distance distribution between oxygen and oxygen among water molecules. Both membranes exhibited peaks of higher amplitude than those of the bulk water case with broad second peaks, as expected for confined water.⁴⁰ Figure 4f shows the radial function between the oxygen and hydrogen for both types of membranes. In this plot, the change in the first-peak to second-peak ratio between the membranes indicates less

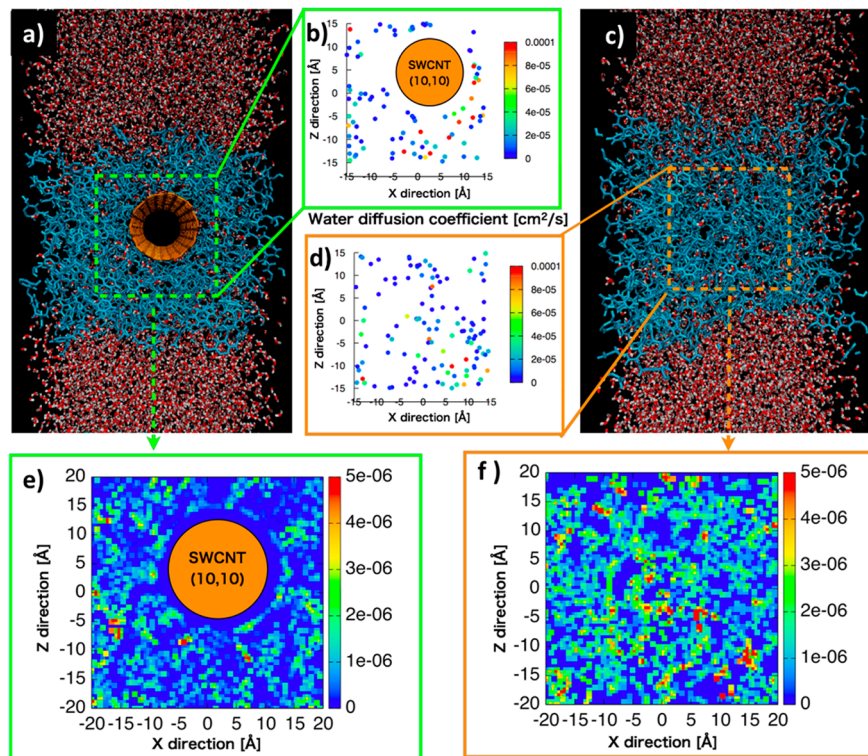


Figure 5. Diffusion coefficient of water and network mobility of PA in the plain PA and SWCNT+PA after hydration with the water membrane are shown. Snapshots of (a) SWCNT+PA and (c) plain PA after hydration are shown. (b and d) Comparison of the water diffusion coefficient for individual water molecules embedded within the membranes. The average network mobility shown during the hydration process in (e) SWCNT+PA and (f) plain PA are shown. The full movie is available in the [Supporting Information](#).

clustering of water in the SWCNT+PA membrane relative to that of the plain PA membrane.

We continued our analysis of the membranes by investigating the diffusion of water molecules in the membrane region during the hydration process using the mean-squared displacement equation ([eq 1](#)) for each atom, as well as the polymer network mobility.

$$D_i = \lim_{t \rightarrow \infty} \frac{1}{6t} (|r_i(t) - r_i(0)|^2) \quad (1)$$

where D_i is the diffusion coefficient for each atom, $r_i(0)$ are the initial spatial coordinates and $r_i(t)$ the spatial coordinates at time t .

[Figure 5a](#) shows a snapshot of the SWCNT+PA membrane, and in [Figure 5b](#), the diffusion coefficients for each single water molecule in this membrane were plotted. Similarly, panels c and d in [Figure 5](#) show the snapshot of the plain PA membrane and the corresponding diffusion coefficient values for the water molecules, respectively. The average diffusion coefficients for the entire areas studied are 3.07×10^{-5} and $3.38 \times 10^{-5} \text{ cm}^2/\text{s}$ for the SWCNT+PA and PA membrane, respectively. Interestingly, despite the higher membrane density, the smaller pore radius in the hydrated state, and steric hindrance of the SWCNT, the water molecules in the SWCNT+PA membrane almost have a similar average diffusion coefficient as that of the plain PA. Indeed, the incorporation of the SWCNT only reduced the water diffusivity by 9.1% while providing mechanical reinforcement to the PA layer. Remarkably, a more robust membrane can potentially be made thinner and used at higher pressures or temperatures, thus improving the permeation flow rate. Even if the SWCNTs act as impermeable

cylindrical objects in the membrane, their effect on increasing the diffusion path is not very large at low loadings. We calculated the effect of nanotubes on the increment of the diffusion path length across the membrane, and the results are plotted in [Figure S7](#). For the case of 15 wt % loading of SWCNT in a 60-nm thick membrane, the increment was only 2%, whereas 15 wt % of MWCNT in a 100-nm thick membrane increased the diffusion path in 5%.

To understand better the effect of the SWCNT on the PA, we analyzed the membrane mobility during the hydration dynamics, and the results are shown in [Figure 5e](#) and compared with that of the plain PA membrane ([Figure 5f](#)). The plots show that the SWCNT+PA membrane has lower network mobility, which is explained by the strong van der Waals interaction of the PA aromatic molecules in the vicinity of the nanotube with the nanotube surface. The average plain PA structure showed an average value of $2.72 \times 10^{-6} \text{ cm}^2/\text{s}$, which decreased to $2.13 \times 10^{-6} \text{ cm}^2/\text{s}$ after the inclusion of the SWCNT. Even though this force decreases swiftly with distance, the highly cross-linked nature of the network efficiently restricted the entire network mobility. In this sense, the SWCNT behaves as a nanoreinforcement that mechanically stabilizes the polymer network. This direct link between network mobility and the nanofiller in PA RO membranes has not been reported to date and might explain similar effects in other nanocomposite PA membranes. The resulting PA network is more rigid and has properties very different from those of the conventional plain PA.

2.4. Effect of Salt on Membrane Hydration. A semiempirical relationship between water and salt sorption with water permeation and salt rejection has long been

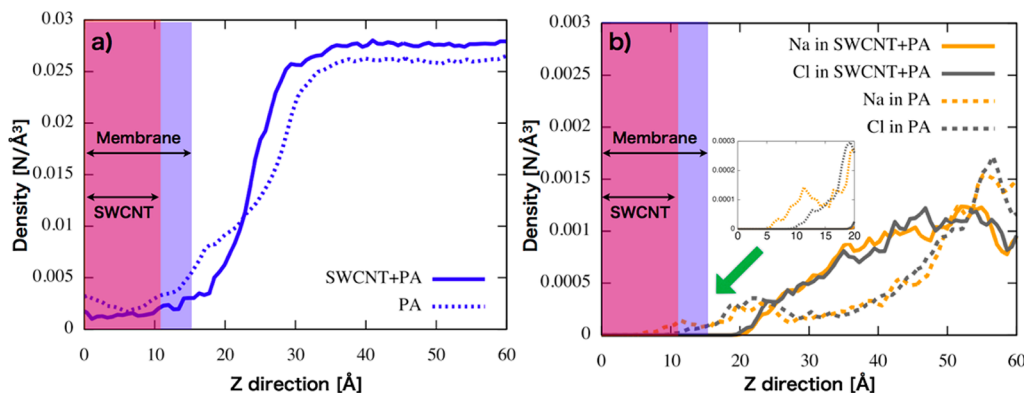


Figure 6. Density profiles of Na, Cl, and water across the membrane, the membrane layer interface, and the salt solution. (a) Water density profile in both membranes and (b) comparison of Na and Cl density profiles. The purple region is defined as the membrane region for both types of membranes, whereas the wine-colored area indicates the position of the SWCNT in the nanocomposite membrane.

known.⁴¹ It is thought that good membranes should show high water adsorption while avoiding the formation of water clusters within the membrane because these clusters allow the formation of ion-transport channels, resulting in high salt permeation. Although the former studies in membrane hydration were experimental, recently, it has become easier to simulate membrane hydration through molecular dynamics. The hydration process is easier to simulate than permeation; thus, the study of membrane hydration through molecular dynamics has become a useful tool for understanding and predicting membrane performance.

Finally, the hydration of both membranes was investigated in simulated seawater solution. In this case, 4000 water molecules were located below the membrane, and simulated seawater, consisting of 4000 water and 40 NaCl molecules (3 wt %), was located on top of the membrane. MD simulations were performed to allow for membrane hydration under a pressure of approximately 4.8 MPa in the seawater side of the membranes. The resulting density profiles of water and salt ions are shown in Figure 6a and b, respectively. The water density profiles (Figure 6a) indicate that hydration of the plain PA membrane in seawater is slightly higher than that of the nanocomposite membrane, as expected from a membrane with a larger average pore-size in the hydrated state. Interestingly, Figure 6b reveals that Na and Cl ions did not permeate through the SWCNT+PA membranes, contrasting with the behavior seen on the plain PA membrane. This ion rejection is most likely caused by the smaller pore size distribution in the hydrated state, as seen in Figure 4c and d, but mainly due to the absence of pores with large radius in the nanocomposite membrane. Indeed, the number of peaks with radii larger than 2.5 Å in SWCNT+PA is smaller than in the plain PA membrane. These pores can easily accommodate the hydrated Cl and Na ion. Thus, the addition of SWCNT to the PA might result in a high salt rejection membrane, suggesting a greater potential for desalination than the plain PA membrane, particularly for membranes used in one-step direct desalination from seawater.

3. CONCLUSIONS

The adsorption of MPD molecules onto the surface of SWCNTs indicates a preferential alignment of the aromatic MPD parallel to the SWCNT axis, and this alignment is induced by the strong van der Waals forces. After polymerization, the polyamide network shows orientation for a total of

two consequent layers, although the effect of the nanotube on the network mobility extends to the whole area studied due to the highly cross-linked nature of the PA structure. Further, the degree of alignment for the first couple of layers is slightly enhanced at greater SWCNT diameters and can possibly be higher in MWCNT where van der Waals forces might be stronger. The effect of restricted network mobility of the SWCNT might be beneficial to increase the salt rejection rate, reduce the creep deformation of the membrane, and extend its use at higher temperatures than those possible in plain PA membranes. The present work on SWCNT+PA nanocomposite membranes suggests potential high performance by the MWCNT+PA nanocomposite RO membrane developed on desalination as well and permeation properties.

4. EXPERIMENTAL SECTION

4.1. MPD Orientation near SWCNTs. In the first stage of our study, we simulated the adsorption and spatial orientation of the MPD molecules on three different types of SWCNTs. Their characteristics are given in Table 2.

Table 2. SWCNT Types Used for Calculations of MPD Adsorption

SWCNT type	diameter (Å)	carbon atoms
(6,6)	8.13	504
(10,10)	13.56	840
(18,18)	24.41	1512

The number of MPD molecules was set to 250 in all cases. To quantify the spatial direction of MPD molecules, we defined the orientation function f as described by eq 2

$$f(r_i) = \left\langle \sum_{j=1}^{n(r_i)} \frac{\cos \theta_{12}}{n(r_i)} \right\rangle \quad (2)$$

where r_i is the distance of an individual MPD molecule to the SWCNT surface, θ_{12} is the angle between the vector from the SWCNT surface to the MPD center of mass and a vector parallel to the hexagonal aromatic ring of the MPD molecule, $n(r_i)$ is the MPD number from r_i to $r_i + \Delta r$, Δr is the calculation mesh (set to 0.2 Å), and $\langle \dots \rangle$ represents the time average. Basically, this function fluctuates from 1 to describe an MPD molecule whose aromatic ring is parallel to the SWCNT surface and 0 for a molecule oriented perpendicularly to the SWCNT surface. In the case of the plain PA, and for the sake of comparison, we assumed that an imaginary SWCNT(10,10) exists

with the PA membrane center and calculated the orientation function according to this assumption.

4.2. Polyamide Network Construction. Aromatic polyamide (PA) membrane models are usually created by the molecular dynamics (MD) method with additional potential or Monte Carlo method.^{16,36} However, we have considered the topological information only as an initial model. The procedure used to construct the cross-linked membrane model is schematized in Figure S5. Briefly, the reactive TMC and MPD moieties are located in the structure, and the coordinates for the acyl chloride or amine functional groups are found. Then, new TMC and MPD molecules are added to the growing PA molecule, generating amide bonds. In the next step, the space coordinates of the newly added molecules are evaluated, and if they overlap with the PA network, then the moiety is detached. This procedure is repeated until the network is built. The algorithm also considers the self-reaction between closely located TMC and MPD groups. If this distance is in the range of $1.6 \text{ \AA} < r < 4.5 \text{ \AA}$, then an amide bond is added and a ring structure is created. In the case of the nanocomposite membrane that includes a SWCNT (SWCNT+PA), the same method was used. Nevertheless, initially, 10 MPD molecules are allowed to equilibrate with the SWCNT by adsorption during the initial state of the procedure. Then, the polymerization proceeds using the same method employed for the plain PA. When the monomers are exhausted, the remaining acyl groups are substituted with OH groups emulating the hydrolysis that occurs in experimental conditions. The initial models obtained after this stage are considered a topological model only and are energetically unstable. Therefore, an MD calculation is performed to obtain the final model in the dry state. To calculate the diffusion length increment due to carbon nanotube addition to the PA matrix, we constructed virtual membranes that are approximately 100- or 60-nm thick loaded with randomly distributed cylindrical objects representing different mass loadings of MWCNT or SWCNT, respectively. Then, we measured 100 diffusion paths across the membrane that started in random places and were perpendicular to the membrane. Whenever a diffusion path was obstructed by a nanotube, the path was adjusted to follow the nanotube surface until the molecule could continue its path across the membrane.

4.3. Molecular Dynamics. MPD Adsorption on SWCNT with and without Water. We performed MPD adsorption simulations with and without water by DL-poly code⁴² and NVT ensemble at 300 K using the Nose–Hoover method.³⁰ The DREIDING⁴³ force field was used for the MPD inner molecules interaction, and the Tersoff potential was used for the SWCNT(10,10). When water molecules were considered, we adopted an SPC/E model.⁴⁴ The interaction between molecules are described by Lennard-Jones (LJ) and Coulomb interactions with the particle mesh Ewald (PME) method. We prepared a simulation box with unit cell (50.0, 50.0, 51.65). Axis of SWCNT was located along z direction. With the water case, 3600 water molecules and 46 MPD molecules were located randomly in the simulation box. All MPD molecules were adsorbed on SWCNT with a MD time of 1.5 ns. IN the case without water, 50 MPD molecules were located randomly. In this case, the MD simulation time was 0.25 ns for all MPD adsorption. We observed that, in the without water case, the calculation was very quick, and the orientation function was similar to that with water; then, to minimize computation time, we continued our calculations of MPD orientation without considering water.

Polyamide Molecular Dynamics. The interactions between MPD and TMC (MPD and MPD, TMC and TMC) are Lennard-Jones (LJ) and Coulomb type. For Coulomb interactions, a particle mesh Ewald (PME) method was used. The atom charges of the MPD and TMC monomers were determined by ab initio quantum chemistry calculation at MP2/6-31G** level, using the NWChem code.⁴⁵ In the case of the cross-linked polyamide, the atom charges were calculated with ANTECHAMBER 1.27 and AM1-BCC partial charges.^{41,46} The interactions between carbon atoms of SWCNT and MPD, or TMC, are LJ only. All LJ parameters were referred to DREIDING parameters.³¹ SWCNT interactions are described by the Tersoff potential,⁴⁷ and all cutoff radii were set to 15.0 Å. The simulations had a time step of 0.1 fs, an equivalent time of 1 ns, and a

simulation time of 3 ns for statistical analysis. For water permeability simulations, water molecule models were simulated using the SPC/E model with the SHAKE algorithm.⁴⁸ The interaction between water and SWCNT or PA are LJ interactions,^{36,49} and the specific case of PA and water molecules uses Coulomb interactions. Simulation of the water-solvated membrane system was performed in the NPT ensemble at 300 K and 1 atm. For pressure control, a graphene sheet was used as a virtual piston. The simulation boxes including water were $L_x = 54.0 \text{ \AA}$, $L_y = 51.58 \text{ \AA}$, and $L_z = 134.5 \text{ \AA}$ in the SWCNT+PA membrane and $L_x = 51.20 \text{ \AA}$, $L_y = 52.40 \text{ \AA}$, and $L_z = 134.0 \text{ \AA}$ in the plain PA membrane.

ASSOCIATED CONTENT

Supporting Information

The Supporting Information is available free of charge on the ACS Publications website at DOI: [10.1021/acsmi.5b06248](https://doi.org/10.1021/acsmi.5b06248).

Additional network models, mechanism paths, electron microscopy images, and structural models ([PDF](#))

Movie showing the comparative hydration dynamics of pure PA and SWCNT+PA membranes in pure water ([MPG](#))

AUTHOR INFORMATION

Corresponding Author

*E-mail: endo@endomoribu.shinshu-u.ac.jp. Tel: 81-(0)26-269-5602.

Author Contributions

M.E. designed the experiment and coordinated the project. T.A., S.T., and R.C.-S. carried out the molecular simulations. K.T. and T.H. carried out the TEM observations. S.I. and T.N. carried out the membrane synthesis. A.T. and T.K. supervised the PA molecular structure design. M.T. supervised SWCNT and membrane molecular dynamics. The manuscript was mainly written by R.C.-S., T.A., and M. E. with contributions of all authors. All authors discussed and gave approval to the final version of the manuscript.

Notes

The authors declare no competing financial interest.

ACKNOWLEDGMENTS

This research was supported by the Center of Innovation Program “Global Aqua Innovation Center for Improving Living Standards and Water-sustainability” from the Japan Science and Technology Agency, JST.

ABBREVIATIONS

RO = reverse osmosis

SWCNT = single walled carbon nanotube

PA = polyamide

MPD = 1,3-diaminobenzene

TMC = 1,3,5-benzenetricarbonyl trichloride

REFERENCES

- (1) Elimelech, M.; Phillip, W. A. The Future of Seawater Desalination: Energy, Technology, and the Environment. *Science* **2011**, *333* (6043), 712–717.
- (2) Shannon, M. A.; Bohn, P. W.; Elimelech, M.; Georgiadis, J. G.; Marinas, B. J.; Mayes, A. M. Science and Technology for Water Purification in the Coming Decades. *Nature* **2008**, *452* (7185), 301–310.
- (3) Greenlee, L. F.; Lawler, D. F.; Freeman, B. D.; Marrot, B.; Moulin, P. Reverse Osmosis Desalination: Water Sources, Technology, and Today's Challenges. *Water Res.* **2009**, *43* (9), 2317–2348.

- (4) Lawson, K. W.; Lloyd, D. R. Membrane Distillation. *J. Membr. Sci.* **1997**, *124* (1), 1–25.
- (5) Wade, N. M. Distillation Plant Development and Cost Update. *Desalination* **2001**, *136* (1–3), 3–12.
- (6) Goosen, M.; Mahmoudi, H.; Ghaffour, N. Water Desalination Using Geothermal Energy. *Energies* **2010**, *3* (8), 1423–1442.
- (7) Qiblawey, H. M.; Banat, F. Solar Thermal Desalination Technologies. *Desalination* **2008**, *220* (1–3), 633–644.
- (8) Cadotte, J. E. Interfacially synthesized reverse osmosis membrane. US Patent 4277344A.
- (9) Kim, C. K.; Kim, J. H.; Roh, I. J.; Kim, J. J. The Changes of Membrane Performance with Polyamide Molecular Structure in the Reverse Osmosis Process. *J. Membr. Sci.* **2000**, *165* (2), 189–199.
- (10) Roh, I. J.; Park, S. Y.; Kim, J. J.; Kim, C. K. Effects of the Polyamide Molecular Structure on the Performance of Reverse Osmosis Membranes. *J. Polym. Sci. J. Polym. Sci., Part B: Polym. Phys.* **1998**, *36* (11), 1821–1830.
- (11) Roh, I. J.; Khare, V. P. Investigation of the Specific Role of Chemical Structure on the Material and Permeation Properties of Ultrathin Aromatic Polyamides. *J. Mater. Chem.* **2002**, *12* (8), 2334–2338.
- (12) Kolev, V.; Freger, V. Hydration, Porosity and Water Dynamics in the Polyamide Layer of Reverse Osmosis Membranes: a Molecular Dynamics Study. *Polymer* **2014**, *55* (6), 1420–1426.
- (13) Murad, S.; Powles, J. G. Computer-Simulations of Osmosis and Reverse-Osmosis in Solutions. *Chem. Phys. Lett.* **1994**, *225* (4–6), 437–440.
- (14) Murad, S. Molecular Dynamics Simulations of Osmosis and Reverse Osmosis in Solutions. *Adsorption* **1996**, *2* (1), 95–101.
- (15) Kotelyanskii, M. J.; Wagner, N. J.; Paulaitis, M. E. Atomistic Simulation of Water and Salt Transport in the Reverse Osmosis Membrane FT-30. *J. Membr. Sci.* **1998**, *139* (1), 1–16.
- (16) Luo, Y.; Harder, E.; Faibis, R. S.; Roux, B. Computer Simulations of Water Flux and Salt Permeability of the Reverse Osmosis FT-30 Aromatic Polyamide Membrane. *J. Membr. Sci.* **2011**, *384* (1–2), 1–9.
- (17) Ding, M. X.; Szymczyk, A.; Goujon, F.; Soldera, A.; Ghoufi, A. Structure and Dynamics of Water Confined in a Polyamide Reverse-Osmosis Membrane: a Molecular-Simulation Study. *J. Membr. Sci.* **2014**, *458*, 236–244.
- (18) Duan, J. T.; Litwiller, E.; Pinnau, I. Preparation and Water Desalination Properties of POSS-polyamide Nanocomposite Reverse Osmosis Membranes. *J. Membr. Sci.* **2015**, *473*, 157–164.
- (19) Chan, W. F.; Chen, H. Y.; Surapathi, A.; Taylor, M. G.; Hao, X. H.; Marand, E.; Johnson, J. K. Zwitterion Functionalized Carbon Nanotube/Polyamide Nanocomposite Membranes for Water Desalination. *ACS Nano* **2013**, *7* (6), 5308–5319.
- (20) Kazemimoghadam, M. Preparation of Nanopore HS Zeolite Membranes for Reverse Osmosis Processes. *Desalin. Water Treat.* **2011**, *30* (1–3), 51–57.
- (21) Azamat, J.; Khataee, A.; Joo, S. W. Separation of a Heavy Metal from Water through a Membrane Containing Boron Nitride Nanotubes: Molecular Dynamics Simulations. *J. Mol. Model.* **2014**, *20* (10), 2468.
- (22) Gong, X. J.; Li, J. Y.; Lu, H. J.; Wan, R. Z.; Li, J. C.; Hu, J.; Fang, H. P. A Charge-Driven Molecular Water Pump. *Nat. Nanotechnol.* **2007**, *2* (11), 709–712.
- (23) Kiani, F.; Khosravi, T.; Moradi, F.; Rahbari, P.; Aghaei, M. J.; Arabi, M.; Tajik, H.; Kalantarnejad, R. Computational Investigation of Carbon Nanotubes-Enhanced Membrane for Water Desalination Based on Flux and Rejection Characteristics. *J. Comput. Theor. Nanosci.* **2014**, *11* (5), 1237–1243.
- (24) Nicolai, A.; Sumpter, B. G.; Meunier, V. Tunable Water Desalination Across Graphene Oxide Framework Membranes. *Phys. Chem. Chem. Phys.* **2014**, *16* (18), 8646–8654.
- (25) Cohen-Tanugi, D.; Grossman, J. C. Mechanical Strength of Nanoporous Graphene as a Desalination Membrane. *Nano Lett.* **2014**, *14* (11), 6171–6178.
- (26) Cohen-Tanugi, D.; Grossman, J. C. Water Permeability of Nanoporous Graphene at Realistic Pressures for Reverse Osmosis Desalination. *J. Chem. Phys.* **2014**, *141* (7), 4.
- (27) Lee, H. D.; Kim, H. W.; Cho, Y. H.; Park, H. B. Experimental Evidence of Rapid Water Transport through Carbon Nanotubes Embedded in Polymeric Desalination Membranes. *Small* **2014**, *10* (13), 2653–60 28.
- (28) Park, J.; Choi, W.; Kim, S. H.; Chun, B. H.; Bang, J.; Lee, K. B. Enhancement of Chlorine Resistance in Carbon Nanotube-based Nanocomposite Reverse Osmosis Membranes. *Desalin. Water Treat.* **2010**, *15* (1–3), 198–204.
- (29) Duan, W. Y.; Dudchenko, A.; Mende, E.; Flyer, C.; Zhu, X. B.; Jassby, D. Electrochemical Mineral Scale Prevention and Removal on Electrically Conducting Carbon Nanotube - Polyamide Reverse Osmosis Membranes. *Environ. Sci.: Processes Impacts* **2014**, *16* (6), 1300–1308.
- (30) Kim, H. J.; Choi, K.; Baek, Y.; Kim, D. G.; Shim, J.; Yoon, J.; Lee, J. C. High-Performance Reverse Osmosis CNT/Polyamide Nanocomposite Membrane by Controlled Interfacial Interactions. *ACS Appl. Mater. Interfaces* **2014**, *6* (4), 2819–2829.
- (31) Shen, J. N.; Yu, C. C.; Ruan, H. M.; Gao, C. J.; Van der Bruggen, B. Preparation and Characterization of Thin-Film Nanocomposite Membranes Embedded with Poly(methyl methacrylate) Hydrophobic Modified Multiwalled Carbon Nanotubes by Interfacial Polymerization. *J. Membr. Sci.* **2013**, *442*, 18–26.
- (32) Tiraferri, A.; Vecitis, C. D.; Elimelech, M. Covalent Binding of Single-Walled Carbon Nanotubes to Polyamide Membranes for Antimicrobial Surface Properties. *ACS Appl. Mater. Interfaces* **2011**, *3* (8), 2869–2877.
- (33) Inukai, S.; Cruz-Silva, R.; Ortiz-Medina, J.; Morelos-Gomez, A.; Takeuchi, K.; Hayashi, T.; Tamioka, A.; Araki, T.; Tejima, S.; Noguchi, T.; Terrones, M.; Endo, M. High-Performance Multi-Functional Reverse Osmosis Membranes Obtained by Carbon Nanotube-Polyamide Nanocomposite. *Sci. Rep.* **2015**, *5*, 10.
- (34) Jiang, L. Y.; Huang, Y.; Jiang, H.; Ravichandran, G.; Gao, H.; Hwang, K. C.; Liu, B. A Cohesive Law for Carbon Nanotube/Polymer Interfaces Based on the van der Waals Force. *J. Mech. Phys. Solids* **2006**, *54* (11), 2436–2452.
- (35) Bhattacharya, S.; Gubbins, K. E. Fast Method for Computing Pore Size Distributions of Model Materials. *Langmuir* **2006**, *22* (18), 7726–7731.
- (36) Harder, E.; Walters, D. E.; Bodnar, Y. D.; Faibis, R. S.; Roux, B. Molecular Dynamics Study of a Polymeric Reverse Osmosis Membrane. *J. Phys. Chem. B* **2009**, *113* (30), 10177–10182.
- (37) Drazevic, E.; Kosutic, K.; Kolev, V.; Freger, V. Does Hindered Transport Theory Apply to Desalination Membranes? *Environ. Environ. Sci. Technol.* **2014**, *48* (19), 11471–11478.
- (38) Singh, P. S.; Ray, P.; Xie, Z.; Hoang, M. Synchrotron SAXS to Probe Cross-Linked Network of Polyamide 'Reverse Osmosis' and 'Nanofiltration' Membranes. *J. Membr. Sci.* **2012**, *421*, 51–59.
- (39) Kotelyanskii, M. J.; Wagner, N. J.; Paulaitis, M. E. Molecular Dynamics Simulation Study of the Mechanisms of Water Diffusion in a Hydrated, Amorphous Polyamide. *Comput. Theor. Polym. Sci.* **1999**, *9* (3–4), 301–306.
- (40) Strathmann, H.; Michaels, A. S. Polymer-water interaction and its relation to reverse osmosis desalination efficiency. *Desalination* **1977**, *21* (2), 195–202.
- (41) Morineau, D.; Alba-Simionesco, C. Liquids in Confined Geometry: How to Connect Changes in the Structure Factor to Modifications of Local Order. *J. Chem. Phys.* **2003**, *118* (20), 9389–9400.
- (42) Smith, W.; Todorov, I. T. A Short Description of DL_POLY. *Mol. Simul.* **2006**, *32* (12–13), 935–943.
- (43) Mayo, S. L.; Olafson, B. D.; Goddard, W. A. DREIDING - A Generic Force-Field for Molecular Simulations. *J. Phys. Chem.* **1990**, *94* (26), 8897–8909.
- (44) Kusalik, P. G.; Svishchev, I. M. The spatial structure in liquid water. *Science* **1994**, *265*, 1219–1221.

- (45) Siepmann, J. I. A Method for the Direct Calculation of Chemical Potentials for Dense Chain Systems. *Mol. Phys.* **1990**, *70* (6), 1145–1158.
- (46) Xiang, Y.; Liu, Y.; Mi, B.; Leng, Y. Molecular Dynamics Simulations of Polyamide Membrane, Calcium Alginate Gel, and Their Interactions in Aqueous Solution. *Langmuir* **2014**, *30* (30), 9098–9106.
- (47) Tersoff, J. Modeling solid-state chemistry: Interatomic Potentials for Multicomponent Systems. *Phys. Rev. B: Condens. Matter Mater. Phys.* **1989**, *39* (8), 5566–5568.
- (48) Hammonds, K. D.; Ryckaert, J. P. On the Convergence of the Shake Algorithm. *Comput. Phys. Commun.* **1991**, *62* (2–3), 336–351.
- (49) Jakalian, A.; Jack, D. B.; Bayly, C. I. Fast, Efficient Generation of High-Quality Atomic Charges. AM1-BCC model: II. Parameterization and Validation. *J. Comput. Chem.* **2002**, *23* (16), 1623–1641.